

The Hydrogen Intensity and Real-time Analysis eXperiment: 256-Element Array Status and Overview

Devin Crichton^{a,b,c,*}, Moumita Aich^{b,c}, Adam Amara^{d,a}, Kevin Bandura^{e,f},
Bruce A. Bassett^{g,h,i}, Carlos Bengaly^{j,k}, Pascale Berner^a, Shruti Bhatporia^l,
Martin Bucher^{m,n,b,o}, Tzu-Ching Chang^p, H. Cynthia Chiang^{q,b}, Jean-Francois Cliche^q,
Carolyn Crichton^{j,b,c}, Romeel Dave^{r,s,i}, Dirk I. L. De Villiers^t, Matt Dobbs^q,
Aaron M. Ewall-Wice^{u,p}, Scott Eyono^{b,c}, Christopher Finlay^{j,i,h,g}, Sindhu Gaddam^{b,c},
Ken Ganga^m, Kevin G. Gayley^v, Kit Gerodias^q, Tim B. Gibbon^w, Austine Gumba^{b,c},
Neeraj Gupta^x, Maile Harris^y, Heiko Heilgendorff^{b,c}, Matt Hilton^{b,c}, Adam D. Hincks^z,
Pascal Hitz^a, Mona Jalilvand^{q,j}, Roufurd P.M. Julie^{aa}, Zahra Kader^{b,c}, Joseph Kania^{ab,f},
Dionysios Karagiannis^s, Aris Karastergiou^{ac,s,ad,ae}, Kabelo Kesebonye^{b,c}, Piyanat Kittiwisit^s,
Jean-Paul Kneib^{af}, Kenda Knowles^{b,c,ae}, Emily R. Kuhn^y, Martin Kunz^j, Roy Maartens^{s,d},
Vincent MacKay^{ag,ah}, Stuart MacPherson^{ai}, Christian Monstein^a, Kavilan Moodley^{b,c},
V. Mugundhan^{b,c,aj}, Warren Naidoo^{b,c}, Arun Naidu^{ac}, Laura B. Newburgh^y, Viraj Nistane^j,
Amanda Di Nitto^q, Deniz Ölçek^q, Xinyu Pan^q, Sourabh Paul^s, Jeffrey B. Peterson^{ak},
Elizabeth Pieters^q, Carla Pieterse^{t,c}, Aritha Pillay^{ai}, Anna R. Polish^y,
Liantsoa Randrianjanahary^s, Alexandre Refregier^a, Andre Renard^{ah},
Edwin Retana-Montenegro^{b,c}, Ian H. Rout^c, Cyndie Russeeawon^{ae}, Alireza Vafaei Sadr^j,
Benjamin R.B. Saliwanchik^{al,y}, Ajith Sampath^{b,c}, Pranav Sanghavi^{e,f}, Mario G. Santos^{s,aa},
Onkabetse Sengate^{am,c}, J. Richard Shaw^{an}, Jonathan L. Sievers^{q,am}, Oleg M. Smirnov^{ae,ad},
Kendrick M. Smith^{ao}, Ulrich Armel Mbou Sob^{ae}, Raghunathan Srianand^x,
Pieter Stronkhorst^{ap}, Dhaneshwar D. Sunder^{b,c}, Simon Tartakovsky^q, Russ Taylor^{aq,s},
Peter Timbie^v, Emma E. Tolley^{af}, Junaid Townsend^s, Will Tyndall^y, Cornelius Ungerer^{c,ar},
Jacques van Dyk^{q,as,c}, Gary van Vuuren^{ai}, Keith Vanderlinde^{ah,z}, Thierry Viant^a,
Anthony Walters^{b,c}, Jingying Wang^s, Amanda Weltman^l, Patrick Woudt^{aq}, Dallas Wulf^q,
Anatoly Zavyalov^z, Zheng Zhang^{m,n}

^aInstitute for Particle Physics and Astrophysics, ETH Zürich, Zürich, Switzerland

^bSchool of Mathematics, Statistics, & Computer Science, University of KwaZulu-Natal, Durban, South Africa

^cAstrophysics Research Centre, University of KwaZulu-Natal, Westville Campus, Durban 4000, South Africa

^dInstitute of Cosmology & Gravitation, University of Portsmouth, Dennis Sciama Building, Burnaby Road, Portsmouth PO1 3FX, UK

^eLCSEE, West Virginia University, Morgantown, WV 26506, USA

^fCenter for Gravitational Waves and Cosmology, West Virginia University, Morgantown, WV 26505, USA

^gAfrican Institute for Mathematical Sciences, 6 Melrose Road, Muizenberg, 7945, South Africa

^hDepartment of Maths and Applied Maths, University of Cape Town, Rondebosch, Cape Town, 7700, South Africa

ⁱSouth African Astronomical Observatory, Observatory, Cape Town, 7925, South Africa

^jDépartement de Physique Théorique, Université de Genève, 1211 Genève 4, Switzerland

^kObservatório Nacional, 20921-400, Rio de Janeiro - RJ, Brazil

^lHigh Energy Physics, Cosmology & Astrophysics Theory Group, University of Cape Town, Cape Town, South Africa

^mUniversité de Paris, CNRS, Astroparticule et Cosmologie, F-75013 Paris, France

ⁿLPENS, Ecole Normale Supérieure, 75005 Paris, France

^oNITheCS, Stellenbosch, South Africa

^pNASA Jet Propulsion Laboratory, California Institute of Technology, Pasadena, CA, USA

^qDepartment of Physics, McGill University, Montreal, Quebec H3A 2T8, Canada

^rInstitute for Astronomy, University of Edinburgh, Royal Observatory, Edinburgh EH9 3HJ, UK

^sDepartment of Physics and Astronomy, University of the Western Cape, Cape Town 7535, South Africa

- ^tDepartment of Electrical and Electronic Engineering, Stellenbosch University, Stellenbosch 7600, South Africa
- ^uDepartment of Astronomy, University of California, Berkeley, CA, USA
- ^vDepartment of Physics, University of Wisconsin-Madison, Madison, WI 53706, USA
- ^wCentre for Broadband Communication, Nelson Mandela Metropolitan University, P.O. Box 77000, Port Elizabeth 6031, South Africa
- ^xInter-University Centre for Astronomy and Astrophysics, Post Bag 4, Ganeshkhind, Pune 411 007, India
- ^yDepartment of Physics, Yale University, New Haven, CT, USA
- ^zDavid A. Dunlap Department of Astronomy & Astrophysics, University of Toronto, 50 St. George Street, Toronto, ON M5S 3H4, Canada
- ^{aa}South African Radio Astronomy Observatory, 2 Fir Street, Observatory, Cape Town, 7925, South Africa
- ^{ab}Department of Physics and Astronomy, West Virginia University, Morgantown, WV 26505, USA
- ^{ac}Astrophysics, University of Oxford, Denys Wilkinson Building, Keble Road, Oxford OX1 3RH, UK
- ^{ad}SKA SA, 3rd Floor, The Park, Park Road, Pinelands 7405, South Africa
- ^{ae}Department of Physics and Electronics, Rhodes University, PO Box 94, Makhanda 6140, South Africa
- ^{af}Institute of Physics, Laboratory of Astrophysics, École Polytechnique Fédérale de Lausanne (EPFL), Observatoire de Sauverny, 1290 Versoix, Switzerland
- ^{ag}Department of Physics, University of Toronto, Toronto, Canada
- ^{ah}Dunlap Institute for Astronomy & Astrophysics, University of Toronto, 50 St. George Street, Toronto, ON M5S 3H4, Canada
- ^{ai}Durban University of Technology, Engineering and the Built Environment, P.O. Box 1334, Durban, 4000 South Africa
- ^{aj}Raman Research Institute, India
- ^{ak}Department of Physics, Carnegie Mellon University, Pittsburgh, PA, USA
- ^{al}Department of Physics, Brookhaven National Laboratory, Upton, NY, USA
- ^{am}School of Chemistry and Physics, University of KwaZulu-Natal, Durban, South Africa
- ^{an}Department of Physics and Astronomy, University of British Columbia, Vancouver, BC V6T 1Z1, Canada
- ^{ao}Perimeter Institute for Theoretical Physics, Waterloo, ON N2L 2Y5, Canada
- ^{ap}Hartebeesthoek Radio Astronomy Observatory, P. O. Box 443, Krugersdorp 1740, South Africa
- ^{aq}Department of Astronomy, University of Cape Town, Cape Town, South Africa
- ^{ar}ArioGenix(Pty) Ltd, Pretoria, South Africa
- ^{as}Pronex Engineering Management Consultants CC, Pretoria, South Africa

Abstract. The Hydrogen Intensity and Real-time Analysis eXperiment (HIRAX) is a radio interferometer array currently in development, with an initial 256-element array to be deployed at the South African Radio Astronomy Observatory (SARAO) Square Kilometer Array (SKA) site in South Africa. Each of the 6 m, $f/0.23$ dishes will be instrumented with dual-polarisation feeds operating over a frequency range of 400–800 MHz. Through intensity mapping of the 21 cm emission line of neutral hydrogen, HIRAX will provide a cosmological survey of the distribution of large-scale structure over the redshift range of $0.775 < z < 2.55$ over $\sim 15,000$ square degrees of the southern sky. The statistical power of such a survey is sufficient to produce ~ 7 percent constraints on the dark energy equation of state parameter when combined with measurements from the *Planck* satellite. Additionally, HIRAX will provide a highly competitive platform for radio transient and HI absorber science while enabling a multitude of cross-correlation studies. In these proceedings, we describe the science goals of the experiment, overview of the design and status of the sub-components of the telescope system, and describe the expected performance of the initial 256-element array as well as the planned future expansion to the final, 1024-element array.

Keywords: 21 cm, intensity mapping, cosmology, dark energy, radio transients, interferometers.

*Devin Crichton, dcrichton@phys.ethz.ch

1 Introduction

In recent years, the statistical distribution of large-scale structure in the late-time universe has been measured with increased precision. Current state-of-the-art measurements primarily come

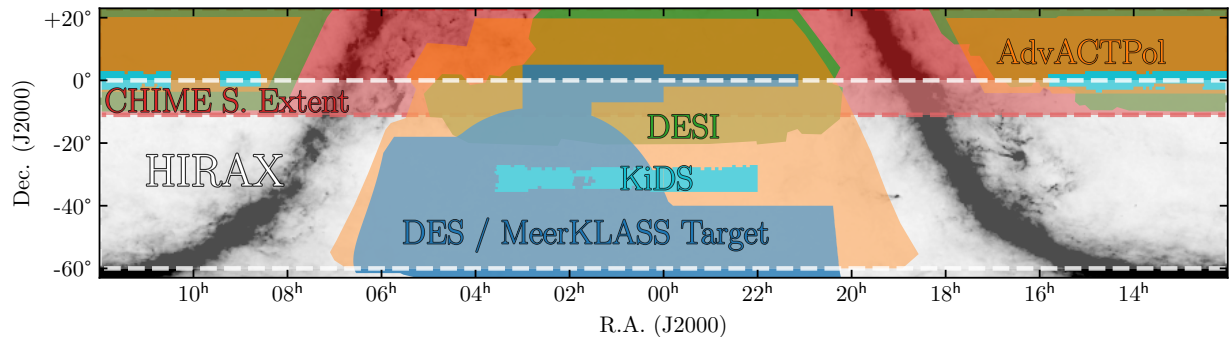


Fig 1 HIRAX will observe $\sim 15,000 \text{ deg}^2$ of the southern sky, shown by the region enclosed by the white dashed lines. The survey footprint overlaps many existing and forthcoming surveys such as those of CHIME,¹¹ DES,⁴ KiDS,⁶ DESI²¹ and Advanced ACTPol.²² The entirety of the sky area shown is contained within the Rubin/LSST²³ survey footprint and is accessible to the SKA²⁴ and its precursors. The background colorscale shows Galactic emission from the *Planck* 353 GHz map.

from baryon acoustic oscillation (BAO) studies from galaxy and Lyman- α surveys as well as weak lensing probes.^{1–7} However, tomographic measurements in the visible/infrared bands become increasingly difficult beyond $z \sim 1$, requiring complex optical systems and long integration times. Intensity mapping with the 21 cm (1420.4 MHz) line of neutral hydrogen has the potential to push beyond these limitations, with observations in the range of $0 < z \lesssim 30$ being achievable with current and planned instruments. The abundance of hydrogen and the optically thin nature of the emission will enable detailed tomographic measurements of the distribution of matter over large, cosmological volumes.^{8–10} In the post-reionisation epoch, by observing the BAO feature in the matter power spectrum, intensity mapping enables cosmological measurements that can break parameter degeneracies in current combinations of early-universe and late-time measurements, as well as constrain the dynamical nature of dark energy over the transition from matter-dominated to dark-energy dominated expansion.

Modern advances in computer and communication hardware as well as the relatively simple, low-frequency receivers required for these observations have motivated the development of large, ~ 100 – 1000 element interferometer arrays such as CHIME,¹¹ CHORD,¹² HERA,¹³ PUMA,¹⁴ and Tianlai.¹⁵ Such telescopes focus their sensitivity on cosmologically relevant angular scales, favouring compact arrays with “redundant” configurations, where the constituent radio telescopes are placed with regular spacing. This type of array architecture additionally provides a natural platform for the detection and monitoring of radio transients, with wide fields of view, fast mapping speeds, and the real-time processing power required for fast radio burst (FRB) detection and pulsar searches, as demonstrated by CHIME in, e.g. Refs. 16–20.

The Hydrogen Intensity and Real-time Analysis eXperiment (HIRAX)²⁵ is a new radio interferometer array that will employ a compact, redundant layout. HIRAX is currently funded for the construction of an initial 256-element array (HIRAX-256) that will comprise a subset of the planned 1024-element array. The telescope will conduct a large 21 cm intensity mapping survey, targeting cosmological constraints on the dark energy equation-of-state parameters, while additionally operating as a platform for transient and HI absorber searches. The cosmological survey requires careful control of systematics due to significant risk of contamination by residuals from foregrounds, which are up to six orders of magnitude brighter in power. The radio transient de-

tection pipeline for HIRAX will focus on searches for FRBs and millisecond pulsars. FRBs are currently under intense study since the nature of their emission processes is not yet understood. HIRAX-256 is expected to detect multiple FRBs per week and future proposed HIRAX outrigger sites with very long baselines (~ 1000 km) will aid in the localisation of FRB detections to within 0.1 arcseconds. Pulsar searches will be performed on beam-formed data at full baseband, allowing for searches over a wide parameter space. Additionally, the flexible digital backend will allow for the monitoring of known pulsars (aiding existing pulsar timing studies) as well as upchannelizing to ~ 3 kHz spectral resolution, which will be used to conduct a blind HI absorber search. Such a search will provide an informative accounting of the state of cold gas in galaxies out to $z \sim 2.5$, encompassing the peak of the global star-formation rate density at $z \sim 2$. Finally, as shown in Figure 1, the $-60^\circ \lesssim \delta \lesssim 0^\circ$ declination range of the HIRAX survey has significant overlap with a range of other large surveys of the southern and equatorial sky, thus enabling a wide range of potential cross-correlation studies. These include optical/infrared galaxy and lensing surveys from eBOSS,²⁶ DES,⁴ KiDS,⁶ HSC,²⁷ DESI,²¹ Rubin/LSST,²³ Euclid²⁸ and Roman²⁹ as well as ground based cosmic microwave background (CMB) surveys from Advanced ACTPol,²² SPT-3G³⁰ and the Simons Observatory.³¹

These science goals are highly synergistic with those of the SKA²⁴ and its precursors. For example, the combined MeerKLASS³² and HIRAX intensity mapping surveys will have the potential to produce a cosmological analysis over a redshift range of $0 \lesssim z \lesssim 2.5$, with contrasting systematic challenges from the differing observing modes and instruments. The blind HI absorber surveys with HIRAX will extend observations beyond the redshift limits of ongoing surveys, such as the MeerKAT Absorption Line Survey (MALS³³), to investigate the relationship between cold atomic gas and the evolution of star formation and AGN activity.

In these proceedings, we present the current status and design of HIRAX-256, as well as the analysis work that has been done to inform these design choices. In Section 2 we introduce the instrument and briefly outline the various sub-components. Section 3 overviews the forecasted cosmological constraints and current analysis methodologies. In Section 4 we describe how forecasts and analysis of simulated data have constrained the design of the instrument, and finally in Section 5 we discuss the current status of the project.

2 Instrument and Subsystems

2.1 Overview

The overall design of HIRAX is driven by optimizing sensitivity to the restricted range of angular scales corresponding to the BAO signature. The BAO science goals thus naturally dictate the high-level instrument configuration. The redshift range $0.775 < z < 2.55$, which captures the onset of the influence of dark energy on the expansion rate at $z \sim 2$, sets the observing frequency range of 400–800 MHz. The 150 Mpc BAO characteristic length corresponds to angular scales of 3° – 1.3° at 400–800 MHz, thus setting a minimum baseline length range of 15–60 m. Along the line of sight, the BAO characteristic length translates into frequency scales of 12–20 MHz, thus setting an absolute minimum requirement of ~ 100 frequency channels over 400–800 MHz. Finally, because the BAO signal is faint (~ 0.1 mK), the instrument must have a large collecting area and low system temperature. The basic HIRAX instrument parameters are summarized in Table 1, and a rendering of the array is shown in Figure 2. The HIRAX array, which will initially consist of 256 elements, will be installed at the South African Radio Astronomy Observatory (SARAO) site in the Karoo



Fig 2 Artist's impression of the HIRAX array in the Karoo desert.

Desert, South Africa, at $30^{\circ}41'47''$ S, $21^{\circ}34'20''$ E. From this site, HIRAX will be able to access $\sim 15,000 \text{ deg}^2$ of the southern sky, as illustrated in Figure 1.

To keep the total data volume at a manageable level, we will take advantage of the redundant configuration of HIRAX to average visibilities within groups of nominally identical baselines. A continuous few-day buffer of the full set of raw visibilities will be stored while the calibration and averaging process is performed, after which the raw data will be deleted. This averaging process is highly sensitive to differences in telescope pairs, since even small mismatches may couple with Galactic emission, which is up to 10^3 times greater in amplitude than the BAO signal, subsequently offsetting the calibration and introducing systematic errors in the observations. Redundant radio telescope arrays that average visibilities early in this way, such as HIRAX, therefore operate in a unique regime that demands precise *control*—not merely characterization—over possible departures from redundancy. The methodology for deriving the HIRAX instrument specifications is discussed in further detail in §4.

The degree to which baselines are redundant and the angular scales over which that redundancy is distributed are important considerations in determining the optimal HIRAX array layout. Evaluating array layouts that strike a balance between redundancy and more uniform uv -plane coverage³⁴ is an active area of study. Key factors favouring maximal redundancy include reduced raw data rate and ease of redundant calibration, whereas key factors favouring less than maximal redundancy include the array chromatic response, taking into account dish-feed and dish-dish coupling across the array, and the impact of instrument errors that cause systematic departures from redundancy.

Figure 3 illustrates the HIRAX signal chain. At the focus of each telescope dish, the incoming radio signals are received and amplified by a dual-polarization active feed, band limited to 400–800 MHz, and converted to optical light with an RF over optical fibre (RToF) transmitter. The optical signals from all dishes are transmitted to a central processing hub and converted back into RF using RToF receivers, passed through a second stage of 400–800 MHz filtering, and then digitized. HIRAX employs ICE boards³⁵ for digitizing and channelizing the RF inputs, and performing the corner turn operation before the data are passed to the GPU X-engine for correlation.

Parameter	Value
Number of dishes	256
Dish diameter	6 m
Dish focal ratio	0.23
Collecting area	7200 m ²
Frequency range	400–800 MHz
Frequency resolution	1024 channels, 390 kHz
Field of view	5°–10°
Resolution	0.2°–0.4°
Target system temperature	50 K

Table 1 HIRAX instrument parameters for the initial 256-element array.

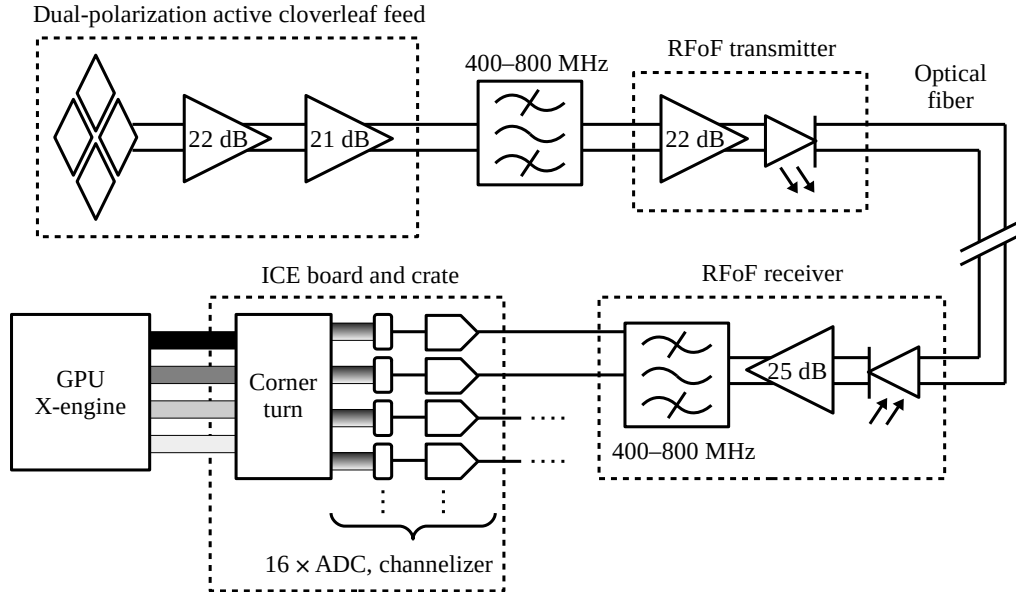


Fig 3 HIRAX signal chain schematic. In each dish, an active dual-polarization feed receives and amplifies incoming radio signals. The signals are filtered, further amplified, and converted to optical light with an RFoF transmitter at the dish focus. Optical fibre transports the signals to an RFoF receiver, which converts the signals back into RF and applies additional amplification and filtering before digitization. An ICE-based system performs the digitization, channelizing, and corner turn. The data are then passed to the GPU X-engine for correlation.

2.2 Dishes and Mounting Structure

Each HIRAX telescope will have a parabolic reflector with a diameter of 6 m and focal ratio of $f/0.23$. The dish size was chosen to maximize collecting area over the minimum baseline lengths, and the low focal ratio allows the entire receiver support structure to sit below the aperture plane, thus reducing cross-talk between neighboring dishes. Each dish will be supported by a mounting structure that is stationary in azimuth and that can be manually repointed in zenith angle over a range of $\pm 30^\circ$ to incrementally build up sky coverage. The HIRAX redundancy requirements have strict implications for the allowed tolerances on the dish surface and the mount alignment, which impact the on-sky beam shape and pointing, respectively. In general, the requirements on dish and mount *precision* are far more stringent than the requirements on *accuracy*. The precision requirements are discussed in further detail in §4.

Dish fabrication methods using composite materials with an embedded reflective layer are well suited for meeting the HIRAX requirements while being cost effective. Fabricating all of the dishes using a small number of molds ensures that variations across the array are kept to a minimum. Composite materials also have high strength-to-weight ratios and are therefore excellent candidates for minimizing gravitational distortion of the dish surfaces as the telescopes are repointed. One prototype composite dish has been installed at the HIRAX test site at the Hartebeesthoek Radio Astronomy Observatory (HartRAO), and other prototyping efforts are currently underway. Further details about the HIRAX prototype dishes and design are available in Ref. 36.

2.3 Dual-Polarization Cloverleaf Feed

HIRAX will use a dual-polarization cloverleaf feed based on the design that was developed for CHIME.³⁷ In contrast to the CHIME feed, which is passive, the HIRAX feed is active. Each polarization of the HIRAX feed consists of a balun that uses an Avago MGA-16116 dual amplifier, providing a gain of 22 dB, and the difference between the outputs are amplified by 21 dB using a Mini-Circuits PSA4-5043+. Each feed is mounted inside a cylindrical can, which circularizes the beam and helps reduce cross-talk. Each feed and can assembly will be supported at the dish focus with a radio-transparent central column that extends upward from the vertex. The column will provide environmental protection by fully enclosing the feed assembly, and the cables will be routed along the boresight axis to minimize their impact on beam asymmetry and sidelobe levels. Measurements of the noise performance of the HIRAX feed and its repeatability is described in Ref. 38.

2.4 Radio Frequency Over fibre System

Signals received by the HIRAX feed are band limited to 400–800 MHz and passed through an additional 22 dB amplification stage before being intensity modulated on an optical carrier at the focus using an RFoF transmitter. Optical fibres carry these signals to a central processing hub, where RFoF receivers convert the signals back into RF. The RF signals are subsequently amplified and filtered again (25 dB gain, 400–800 MHz) before being passed to the digitizer. For the long length of the HIRAX cable runs from the telescopes to the central hub, especially looking ahead to the planned 1024 element array, the combination of RFoF electronics and optical fibres provide a more cost-effective solution than copper coaxial cables. The RFoF transmitter and receiver design is based on technology that was developed by CHIME³⁹ (although ultimately unused in the final experimental configuration). The transmitter contains a laser diode (AGX Technologies,

FPMR3 series¹) that is intensity modulated by the incoming RF signal, and the receiver contains a photodetector (AGX Technologies, PPDD series²) that converts the transmitted optical signal into RF.

2.5 ICE-based F-Engine

The digital back end for HIRAX consists of an FX correlator, with the F-engine comprised of an ICE-based digitisation and channelisation system.^{35,40} The F-engine for HIRAX-256 will be made up of 32 ICE boards, each processing 16 inputs from 8 dual-polarisation feeds. These ICE boards are contained in two ICE crates, each hosting 16 boards. Briefly, the ICE boards use FPGA-based electronics to digitize the incoming signals from the RFoF system at a precision of 8 bits over the full 400 MHz of bandwidth. For the channelisation step, these digitised signals are processed by a polyphase filter bank and FFT based pipeline, producing the 1024 frequency channels (390 kHz wide) that are passed to the correlator. This system also performs the real-time corner-turn operation, which arranges the outgoing data such that each node of the X-engine receives data streams from all inputs over the subset of the bandwidth to be processed by that node. These streams are transferred to the GPU-based X-Engine over a dedicated 40 Gbps network. For the 1024 element array, this system will be scaled up to 128 ICE boards and 8 ICE crates. For HIRAX-256, this system will process an incoming bandwidth of 1.65 Tbps, with the 1024 element being capable of processing 6.6 Tbps.

2.6 GPU Correlator

The HIRAX-256 X-engine is a dense, GPU-based system consisting of 8 nodes, each processing 128 channels or 50 MHz of bandwidth. These nodes will perform full, N^2 , correlation of the incoming data streams from all 512 inputs using a pair of NVIDIA A40 GPUs in each node. The full specifications of each of these correlator nodes is shown in Table 2.

Parameters	Value
Motherboard	GIGABYTE G482-Z52
Processor	2 × AMD EPYC™ 7452, 32 cores each
RAM	1TB
GPU	2 × NVIDIA A40, PCIe 4.0
F-Engine Network	4 × SILICOM PE31640G2QI71-QX4 - 2 × 40 Gbps
Outgoing Data Network	2×25 Gbps

Table 2 HIRAX-256 correlator node specifications. The HIRAX-256 X-engine is comprised of eight these nodes.

This system will produce raw visibility data for each baseline with an integration time of ~ 10 s. Additional outputs from these nodes will include formed beams for the FRB and HI absorber search pipelines as well as for the pulsar search and monitoring systems. This system represents a very dense and powerful correlator, processing 1.6 Tbps of data in a single rack, eight times more bandwidth per node than the CHIME X-engine.⁴¹ This has largely been enabled by making use of the increased I/O performance of PCIe 4.0 for both the GPU and network card interconnects. The X-engine makes use of the *kotekan*^{42,43} software also used by CHIME and CHORD. The

¹<http://www.agxtech.com/PDF/FPMR3+w+Isolator+Rev1.9.pdf>

²<http://www.agxtech.com/PDF/PPDA+R5.6.pdf>

correlator will be scaled up for the 1024-element array, potentially with an even denser layout depending on hardware developments.

2.7 On-site Science Data Processing

Both the visibility data and the beam-formed data from the X-engine will be sent to the on-site science data processing (SDP) system. This system will handle the initial calibration and baseline stacking operations for the cosmological analysis, produce data products for the HI absorber studies and perform the real-time transient searches. Additionally, it will manage and accumulate incoming housekeeping data streams for later use. Reduced data products will be synchronised to off-site computing centres for further processing and long-term storage.

3 Data Analysis Methodology

3.1 Cosmological Survey

HIRAX will operate as a survey instrument to map the large volumes required for precise measurements of the BAO signal. The 21 cm cosmology science goals largely drive the system requirements (§4) for the array as a whole and the constituent telescopes. Here, we begin by outlining the top-level survey parameters that are required to meet the HIRAX BAO science goals.

To reduce cosmic variance, HIRAX will survey $\sim 15,000 \text{ deg}^2$ from declinations $-60^\circ \lesssim \delta \lesssim 0^\circ$ (Figure 1) over a four year period with an observing efficiency of $\sim 50\%$. The time per pointing will be chosen to deliver a survey sensitivity uniform in declination to within 1.5%. To probe the 21 cm power spectrum on BAO scales requires sensitivity to radial wavenumbers in the range $0.03 < k_{\parallel} < 0.2 \text{ Mpc}^{-1}$, which can be achieved with the specified bandwidth and channelisation, and sensitivity to transverse wavenumbers in the range $0.05 < k_{\perp} < 0.16 \text{ Mpc}^{-1}$, which can be achieved with baseline separations covering a minimum range of 8 m to 110 m, as can be seen in Figure 4(a). The HIRAX survey sensitivity is shown in Figure 4(b), which demonstrates that HIRAX is optimised to measure BAO scales where it is competitive with other planned intensity mapping and galaxy redshift surveys. For more details on the calculation of these sensitivity estimates, see Refs. 9, 44.

3.1.1 Fisher Forecasts

We evaluate the cosmological constraints that can be achieved with HIRAX using the Fisher forecast method following the approach of Ref. 9. For reviews on observational approaches to constraining cosmological parameters with BAO measurements, see Refs. 45–47. Our analysis is restricted on small scales to linear modes, on large transverse scales by the minimum baseline length, and on large radial scales by filtering of foreground modes below $k_{\parallel}^{FG} \sim 0.01 \text{ Mpc}^{-1}$. In Figure 5(a) we show forecasts for the measurement of the BAO signal in the power spectrum, demonstrating that HIRAX should resolve this feature with high significance. This in turn leads to percent level constraints on the volume-averaged distance measure, $D_V(z) = [czD_M^2(z)/H(z)]^{1/3}$, in several redshift bins as shown in Figure 5(b). Also shown in Figure 5(b) is a compilation of recent BAO constraints from SDSS galaxy, quasar and Lyman- α surveys.^{1, 48–55}

We explore cosmological parameter constraints for three different cosmological models, ΛCDM , $w\text{CDM}$ and $w_0w_a\text{CDM}$. Here $w\text{CDM}$ allows for variation in a fixed dark energy equation-of-state parameter, w , while $w_0w_a\text{CDM}$, fits for an evolving equation-of-state $w(a) = w_0 + (1 - a)w_a$,

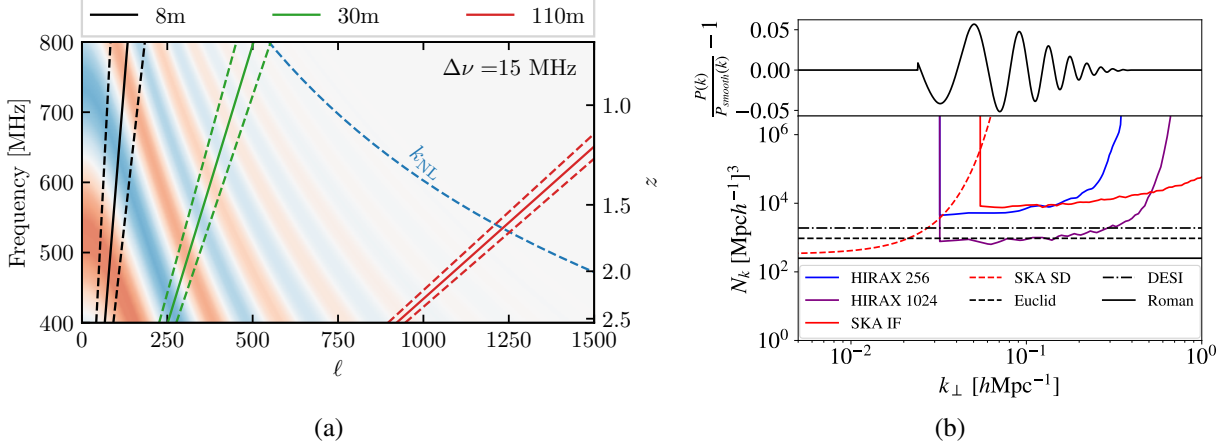


Fig 4 (a) Angular scales accessible to HIRAX baselines as a function of frequency. The background colour scale represents the BAO feature in the 21 cm power spectrum assuming line-of-sight modes, k_{\parallel} , corresponding to correlations over 15 MHz in frequency. The blue curve shows approximately where non-linear effects become significant. This demonstrates the importance of HIRAX’s short baselines, and hence compact layout, for measuring the BAO feature. (b) Comparison of HIRAX’s power spectrum sensitivity as a function of k_{\perp} with that of SKA-MID surveys, in single dish (SD) and interferometer (IF) mode, shown alongside shot noise estimates from upcoming spectroscopic galaxy surveys from DESI, Euclid and Roman. The upper panel shows the BAO feature in the power spectrum as a function of k_{\perp} at $z = 1.2$. Differences in sensitivity due to different survey areas, and hence cosmic variance contributions, are not accounted for here.

as in Ref. 45. Marginalized constraints on a subset of the full parameter set are shown in Table 3 for the HIRAX 256-element and 1024-element arrays including priors based on constraints from the *Planck* Satellite.⁵⁶ These are compared to current state-of-the-art constraints from the eBOSS cosmology analysis,² which are combined with constraints from *Planck*, Pantheon SNe Ia⁵⁷ and DES Y1.⁵⁸

In Figures 5(c) and 5(d) we show marginalized parameter contours for the dark energy equation-of-state parameters as well as large-scale structure parameters Ω_M and σ_8 , respectively, for both the HIRAX 256-element and 1024-element arrays with *Planck* priors. The computed dark energy figures of merit (FoM⁴⁵), corresponding to the inverse of the area enclosed by the 68% confidence contours in the marginalized $w_0 - w_a$ constraints, are 60 for HIRAX-256 and 360 for HIRAX-1024. This is competitive with other planned dark energy experiments.⁹ We note that the *Planck* prior dominates the Ω_M constraint but that the HIRAX 1024-element array, in particular, can further constrain Ω_M and σ_8 .

3.1.2 Cosmological Analysis Pipeline Status

We can obtain more realistic forecasts for HIRAX 21 cm power spectrum constraints using detailed telescope simulations. We adopt the m -mode approach,^{59–61} which is appropriate for a drift-scan instrument such as HIRAX. Decomposing daily scans into m -modes along the sidereal time direction allows us to decouple these modes and analyse them independently, which makes the analysis of large arrays computationally tractable. The simulated visibility, $\mathbf{v} = \mathbf{B} \mathbf{a} + \mathbf{n}$, can be written, for all baselines and frequencies, as a sum of the sky signal, \mathbf{a} , processed by the instrument response or so-called beam transfer matrix, \mathbf{B} , and instrument noise, \mathbf{n} . The beam transfer matrix encodes

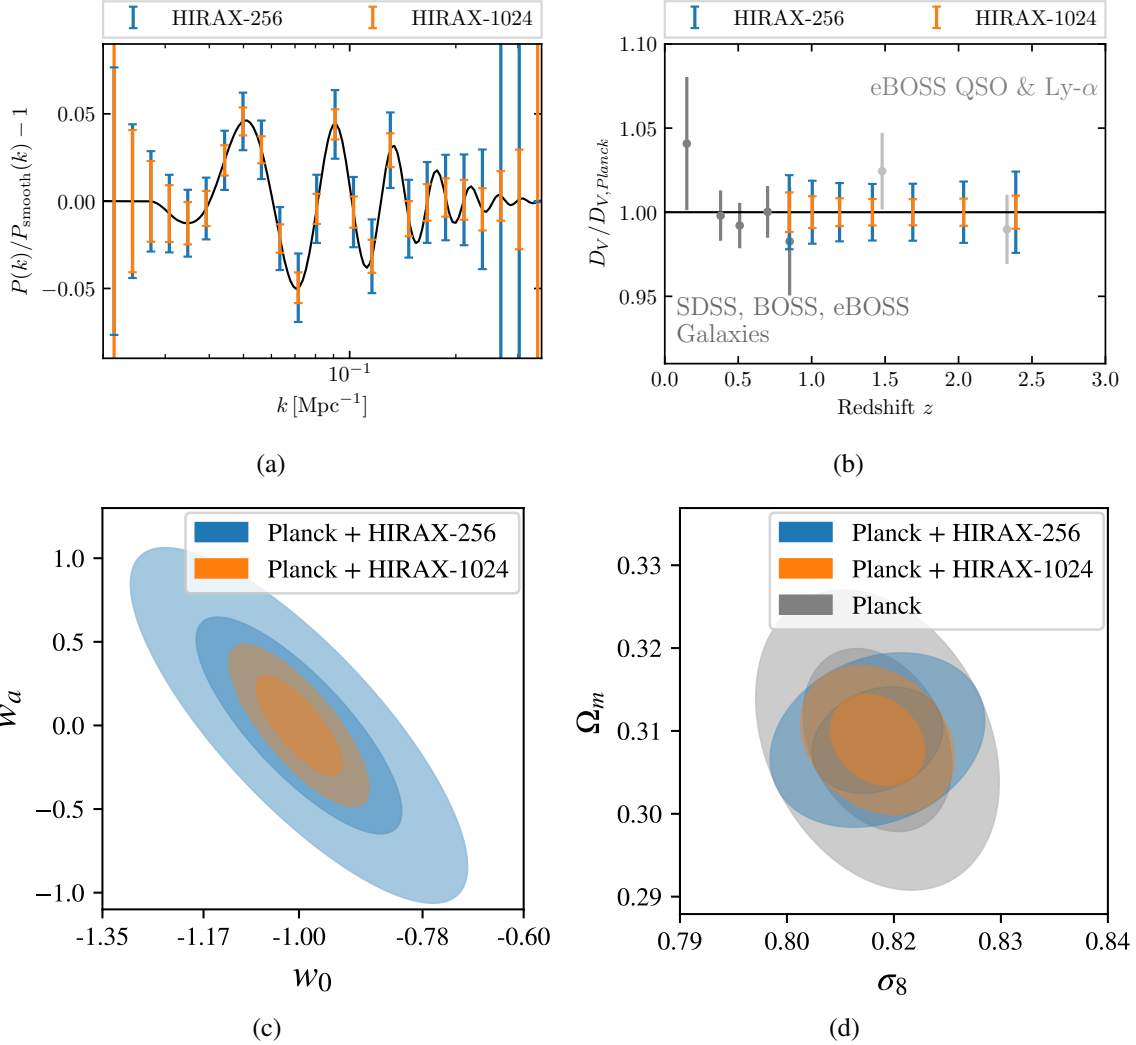


Fig 5 Forecast constraints on (a) the BAO feature of the matter power spectrum, (b) distance scale, D_V evolution, (c) dark energy equation of state parameters w_0 and w_a , (d) large-scale structure parameters σ_8 and Ω_M , for HIRAX-256 and HIRAX-1024. Parameter contours shown represent 68% confidence intervals and, for the parameter constraints, a prior based on *Planck*⁵⁶ results has been added. We note that the change in degeneracy direction for the Ω_M and σ_8 contours between HIRAX-256 and HIRAX-1024 is due to the different relative contributions of the *Planck* prior to the combined constraints.

HIRAX-256 + <i>Planck</i>	σ_8	Ω_Λ	w_0	w_a
Λ CDM	0.00441	0.0039	-	-
w CDM	0.0047	0.0042	0.0739	-
w_0w_a CDM	0.0053	0.0043	0.1223	0.4332
HIRAX-1024 + <i>Planck</i>				
Λ CDM	0.0027	0.0034	-	-
w CDM	0.0028	0.0036	0.0316	-
w_0w_a CDM	0.0038	0.0037	0.0506	0.1965
eBOSS + <i>Planck</i> + SNe Ia + Lens.				
Λ CDM	0.0056	0.0047	-	-
w CDM	0.0092	0.0066	0.027	-
w_0w_a CDM	0.0093	0.0069	0.073	0.5200

Table 3 Marginalized 68% cosmological parameter forecast constraints for the HIRAX experiment compared to current eBOSS² results for Λ CDM, w CDM and w_0w_a CDM cosmologies.

information about the telescope beam and pointing, the baseline layout, and the instrument noise. Here, we consider a Gaussian primary beam but directivities estimated from electromagnetic simulations of the HIRAX antenna³⁶ can also be used in the simulation pipeline. The input sky model comprises simulated 21cm fluctuations with Gaussian statistics and simulated Galactic and extragalactic foregrounds. Currently, these are generated using Gaussian random field realisations of an input 21 cm power spectrum as well as a Galactic foreground model based on that of Ref. 62 with the large-scale spatial distribution of the signal constrained to be similar to that of the Haslam 408 MHz map.⁶³ Future efforts include making use of a more sophisticated signal model based on an empirical HI halo model applied to n -body simulations. Given an instrument model and survey specification, the beam transfer matrix can be computed and is used to generate synthetic visibility data. In the results shown here, we use a compact grid of 7×7 dishes (covering the most cosmologically relevant angular scales) and assume a survey conducted over declinations from -40° to -20° through 7 repointings of the array. The noise is scaled such the the redundancy of the baselines of this 7×7 sub-array are equivalent to that of the 1024 element array with a survey length of four months of integration time per-pointing.

The process of estimating a power spectrum from simulated data is adapted closely from Ref. 60 but we briefly outline it here. In the results shown here, the simulated visibilities are assumed to have negligible calibration residuals but the inclusion of a realistic calibration pipeline and handling for data excised due to, e.g., radio-frequency interference, is being developed. The visibility dataset is then compressed by filtering out modes that the HIRAX baselines are insensitive to using singular value decomposition. The next step involves deprojecting galactic and extragalactic foregrounds, which is the main challenge for a detection of 21cm intensity fluctuations. Foreground removal relies on smooth spectral behaviour of the foregrounds and involves high-pass spectral filtering of the data to retain primarily the high-frequency spectral 21cm modes. Here, we apply a Karhunen–Loève filter based on an ideal instrument with perfect statistical knowledge of the foregrounds. The power spectrum, binned in k_{\parallel} and k_{\perp} , is then estimated from the filtered data.

The plots in Figure 6 show examples of the estimated power spectra constraints using the m -mode approach for a Gaussian beam in four different uniform frequency bands. In this case, the mixing matrix for an unwindowed estimator is used. See Ref. 61 for a detailed discussion on

different quadratic power spectrum window functions. At the relevant scales of interest as mentioned above and depending on frequency channel considered, we expect to recover the binned power spectrum with relative error from 5% to 8% in the approximate range of $0.05 < k < 0.10 \, h \, \text{Mpc}^{-1}$, noting that the set of baselines considered in these simulations also affects these limits. A minimum-variance power spectra estimator reduces the uncertainties by about a factor of two, at the price of a more complicated correlation structure between the bins. In future work, estimated cosmological constraints will be derived from these power spectrum estimates, and contrasted with the Fisher matrix results in Section 3.1.1.

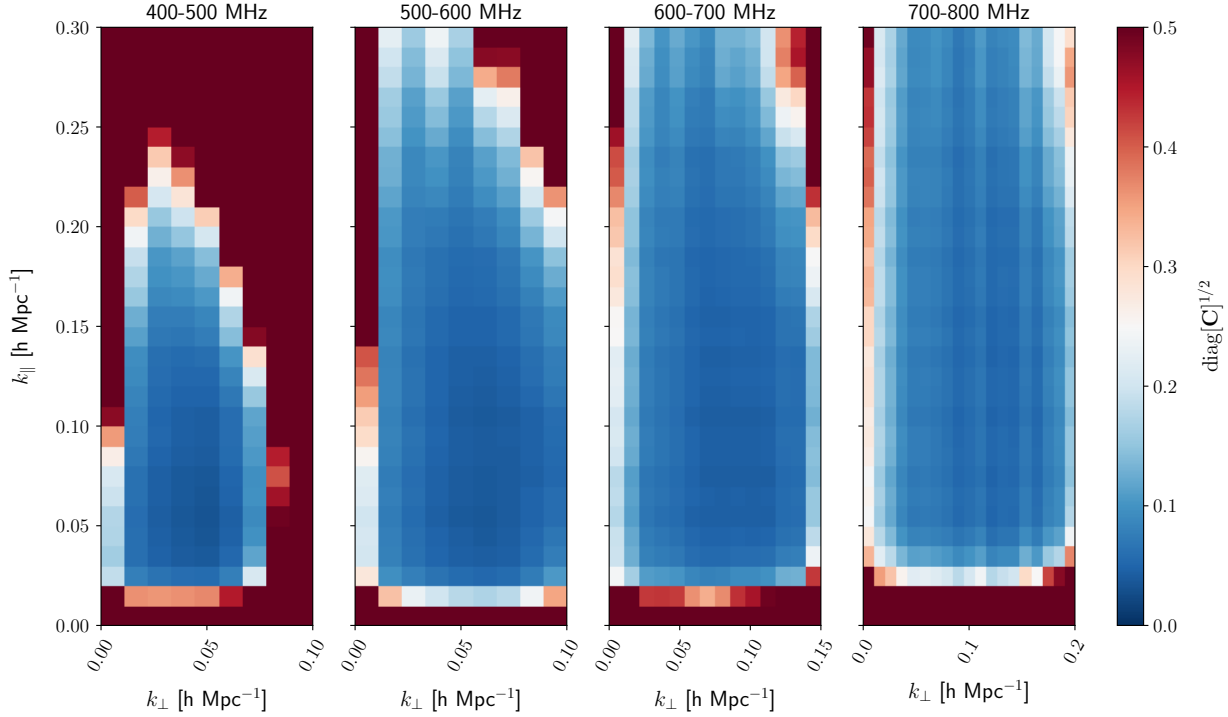


Fig 6 Estimated relative errors in recovered $P(k_{\parallel}, k_{\perp})$ band-powers (from diagonal elements of the derived covariance matrices) over 100 MHz sub-bands spanning the HIRAX bandwidth using the m -mode pipeline. A foreground filter has been applied here assuming ideal knowledge of the instrument.

3.1.3 Systematics Analysis

We have additionally extended the above analysis to examine the effect of unmodeled systematics on the extraction of accurate power spectra. This involves injecting systematic perturbations to the simulated visibilities by assuming distributions of systematic parameters that affect the primary beam, pointing or array layout of the simulated telescope. For the primary beams, electromagnetic simulations of the HIRAX dish-feed systems have been performed,³⁶ including parameter sweeps of physical tolerances of the system under investigation such as feed positioning relative to the dish. Linear models for the perturbations arising from small changes in these tolerances on the beam directivities are then constructed and propagated to the visibilities which are run through the power spectrum estimation pipeline. For layout-based effects such as errors in dish positioning, a similar approach is used where the linear order perturbation on the visibilities due to these uncertainties are propagated through the pipeline. In both cases care is taken to keep track of systematic correlations

between baselines due to sharing systematics from the same dishes. This analysis was used to inform aspects of the system level requirements outlined below, in Section 4.

3.2 Beamforming and Real-time Analysis

HIRAX will sum the channelized baseband data from the array elements to form beams on the sky for use in the transient/FRB, pulsar, and HI absorber searches. The HIRAX beamforming will be fully described in future work, but we provide a brief overview here.

For a calibrated, planar array, the summing reduces to a Fourier transform, where each location on the sky corresponds to a frequency-dependent k . For regularly spaced antennas, Fast Fourier transforms (FFTs) can be used at single frequencies. However, FFTs naturally pick out integer values of k and therefore require additional steps to align the beams across frequencies. Alternatively, one can directly sum the antenna data in a slow Fourier transform. For a close-packed array, there are roughly as many independent beams inside the primary beam as there are antennas. In the simplest implementation, each beam is the sum over n antennas, and with n beams, the total computational cost becomes an order n^2 matrix multiplication. The visibilities already cost n^2 to generate, and so the brute-force beamforming at worst increases the computational burden on the correlator by a constant, order-unity factor. Modern GPUs are sufficiently performant at low bit-depth matrix multiplications that the brute force beamforming is attractive for a 256-element array. For 4-bit operations, the NVIDIA RTX 3090 as well as the NVIDIA A40s in use in the HIRAX-256 X-engine are capable of over 500 TOPS. On paper, a single GPU has enough processing power to form 256 formed beams from 256 HIRAX antennas, and preliminary GPU kernels are within a factor of two of the theoretical limit.

With the decision to use a brute-force beamformer, we can now describe how the HIRAX beamforming will work. The beam-crossing time is relatively short for HIRAX (~ 1 minute) and so we will use tracking beams that follow sources as they transit the primary beam. The RMS per-antenna errors introduced by using 4-bit arithmetic are $\sim 3^\circ$ with an RMS amplitude fractional error of 0.035. Since the data from the F-engine arrive as 4-bit integers, and the errors introduced by 4-bit beamforming are small, we plan to use 4-bit arithmetic to do the beamforming. The beamforming phases will be updated approximately every second. We plan to beamform the intensity data only, using both XX and YY polarization, and do not plan to form real-time cross-polar beams. Since many scientific uses of the formed beams require higher frequency resolution than that provided by the F-engine, the formed beams will be upchannelized (see, e.g., Refs. 64, 65) before being squared and summed to produce high frequency-resolution power beams. These upchannelized beams can then either be integrated in the X-engine for the 21cm absorber search, or passed to the FRB back-end for the FRB search. We additionally will send a small number (~ 10) of non-squared beams to the pulsar back-end for the pulsar search. This gives the pulsar back-end the option of carrying out coherent de-dispersion for millisecond pulsar searches. The utility of HIRAX-256 for pulsar studies is still under study but we expand upon the planned FRB survey below.

3.2.1 Fast Radio Burst Survey

The HIRAX fast radio burst (FRB) survey will use the search pipeline developed for CHIME.⁶⁴ Briefly, the formed, upchannelized beams will be sent to a separate search engine, where they will be incoherently searched for transient events. The search will be carried out by a computationally efficient tree-dedispersion algorithm. Detected FRBs will be flagged, and baseband data will be

written to disk for off-line analysis. The instantaneous detection threshold will be around 10σ , though the exact threshold will need to be tuned on-site and will depend on the false positive rate from local RFI. At 256 dishes, HIRAX has similar collecting area and sensitivity to CHIME, and so we expect the redshift and DM distributions will be similar to the CHIME FRB catalog.¹⁹ With a smaller field of view, we expect an event rate roughly half of CHIME’s, or about 1 FRB per day.

We will build a minimum of two outrigger stations in order to localize FRBs detected by HIRAX to sub-arcsecond accuracy. The central goal is to localize the FRBs to within a host galaxy for the large majority of HIRAX FRBs. Additionally, with ~ 1000 km baselines, we hope to localize FRBs to tens of milliarcseconds (mas) for studies of FRB environments within their host galaxies. Bandwidth constraints prevent us from continuously streaming baseband data, so the outriggers will store 1-2 minutes of baseband data in memory (45 GB/s/dish required). When the core detects an FRB, it will send a trigger to the outriggers that will then write their baseband data to disk, for off-line correlation. Post-processing of the core data will typically result in a higher SNR than the initial detections. Reasons include the ability to reform a beam directly on the FRB, coherently de-disperse the data, and expend more effort on RFI mitigation. We expect 15σ to be typical for the post-processed SNR. We target 5σ detections between the core and each outrigger station, which results in outrigger station sizes of 16-24 dishes. At a fixed false-positive rate, there is an increase required in the SNR due to the possibly large phase space over which one is searching for possible FRBs. For 2-dimensional searches using narrow-band, very long baseline interferometry data, this factor can be large. However, since we are targeting a detection by each station when correlated against the core, the result is a single timing offset from broad-band data, so calculations show the phase-space effect is small for HIRAX. Further, the bulk of the expected false positives arise from small enough timing errors that we would still localize the FRB to the correct galaxy.

Localizations will be fundamentally tied to astronomical calibrators, and we plan to be able to calibrate using observations up to ~ 1 hour after the FRBs occur. We have demonstrated moderately-priced off-the-shelf clock systems that are capable of holding the sub-ns timing accuracy we need on multi-hour timescales.⁶⁶ At HIRAX frequencies, ionospheric corrections are important, and we plan to use a combination of astrometric calibrators, GNSS satellites, and real-time publicly available ionospheric maps. The worst-case scenario of using publicly available ionosphere maps/models corresponds to a typical uncertainty of a few tenths of a TEC unit,³ which translates to roughly 1 nanosecond. For outrigger separations of ~ 1000 km, this corresponds to a 60 mas error, and so we do not expect the ionosphere to limit our ability to assign FRBs to host galaxies.

4 Instrument Requirements

With the science requirements and analysis methods described in §3, we can now define the following high-level system requirements for the HIRAX array. The system requirements are derived by propagating the higher level science requirements, starting from the top-level requirement on the dark energy FoM, to lower level system requirements based on the simulations methodology described in §3. The survey and array layout system requirements were described in §3.1, and here we focus on the requirements for the ensemble of telescopes comprising the array. Since there are

³The total electron content or TEC of the ionosphere is reported in units of $10^{16}e^-/m^2$. 1 TEC unit corresponds to a DM of 3.3×10^{-7} .

typically multiple system requirements that are derived from any given individual science requirement, we consider tradeoffs in tolerances for the system requirements to allocate the error budget. Across the HIRAX array, we find that the gains must be stable to 1% over 1-minute integrations across the full bandwidth, relative bandwidths must be stable to 0.75% over the beam crossing time, and the tolerance on the primary beam FWHM must be 0.05% across the full bandwidth. In addition, the dishes should have an aperture efficiency of 0.7, the antenna cross-talk should contribute an excess noise level of no more than 10 K on the two shortest dish separations, and the antenna spill should have a maximum noise level of 5 K at 400 MHz, increasing to 10 K at 800 MHz. Finally, telescope pointing and positioning must be repeatable across the array: we require that the dish boresight vectors must be parallel within 5' RMS, the foci of all dishes must lie in a plane with < 5 mm RMS deviation orthogonal to the plane, and the foci must form a regularly spaced grid with separation distances precise to < 2.5 mm RMS. We note that the analyses used to derive these constraints were based on science targets for the 1024-element array as the requirements will be fixed across the expected array deployments.

The system requirements for the array as a whole form the foundation for defining more specific requirements for the HIRAX telescope mechanical structure, comprising the dish, mount, and receiver support structure. In total, we have defined over 60 specifications that are discussed in detail in the HIRAX telescope mechanical assembly requirements document, which is available online.⁴ Broadly speaking, tolerances related to redundancy fall into two general categories: pointing or positioning error, and beam error. Pointing and positioning errors are analyzed with a simple geometric model of the telescope to compute the error stackup. Starting with the requirements for boresight vector parallelism and foci positioning within a plane, the error budget is allocated to various telescope sub-components in accordance with the mechanical difficulty of meeting each target. The telescope parameters that are governed by this geometric error stackup include the dish vertex position relative to the elevation axis, orthogonality of the dish boresight vector and elevation axis, position and alignment angle of the elevation axis within the array, and the elevation pointing angle. Errors in the beam shape are assessed with electromagnetic simulations of the dish, receiver, and receiver support structure. We use CST Studio Suite⁵ to simulate the impact of the receiver position with respect to the dish focus, receiver orientation angle relative to the boresight vector, and deviations in the dish surface with respect to the average best-fit paraboloid. Table 4 summarizes the target precision values for the most important telescope mechanical parameters.

5 Current Status and Conclusions

The design of most aspects of the 256-element HIRAX deployment have been finalised and site development is expected to commence in 2022. Currently, multiple hardware testing activities are underway, with instrumented prototype $f/0.38$ and $f/0.25$ dishes deployed at HartRAO for RF front-end characterisation, and parallel efforts in progress at Dominion Radio Astrophysical Observatory and the Green Bank Observatory. Beam characterisation analyses using drone-based and holographic measurements are being carried out. The design of the F- and X-engine systems are complete and the 256-element X-engine is assembled, with one node deployed at the Bleien Observatory for trial operation using on-sky data. A significant milestone has been reached in

⁴https://hirax.ukzn.ac.za/wp-content/uploads/2021/08/HIRAX_REQ001_002_V1_Baselined-signed.pdf

⁵<https://www.3ds.com/products-services/simulia/products/cst-studio-suite/>

Telescope mechanical parameter	Target precision (RMS)
Receiver position relative to focus	0.5 mm
Receiver orientation relative to boresight vector	2.5' polar and azimuthal
Dish surface deviations	1 mm
Dish vertex position relative to elevation axis	1 mm
Orthogonality of boresight vector and elevation axis	1'
Elevation axis position within the array	0.5 mm in array plane 1 mm out of array plane
Elevation axis alignment within the array	1'
Elevation pointing angle	1'

Table 4 Target precision values for HIRAX telescope mechanical structure

the finalisation of the specification for the telescope mechanical system, with the expectation that initial deployed dishes making use of the final design should be assembled for testing in 2022.

HIRAX-256 will be a powerful instrument for 21 cm cosmology, radio transient, and HI absorber science. While much emphasis has been placed on the control of systematics from *a priori* studies, we expect the analysis of the initial on-sky data to be extremely informative for progressing the analysis techniques in use as well as the design of future 21 cm experiments.

Acknowledgments

This work is based on the research supported in part by the National Research Foundation of South Africa (Grant Numbers 98772, 128919, 107797, 120809, 120700) and in part by grant numbers 200021_192243, 200020_182231, IZLSZ2_170907, 20FL21_186180 and 20FL20_201479 from the Swiss National Science Foundation. AR, DC, TV, CB, CF, MK, VN, AVS, ET, and JPK acknowledge funding by the Swiss National Science Foundation. KM acknowledges support from the National Research Foundation of South Africa. AW and SB acknowledge support from the South African Research Chairs Initiative of the Department of Science and Technology and National Research Foundation and from a VC 2020 Future Leaders award. RM, DK, LR, DdV and CP are supported by the South African Radio Astronomy Observatory (SARAO) and the National Research Foundation (Grant No. 75415 and 75322) and RM is also supported by the UK STFC Consolidated Grant ST/S000550/1. WN and DC acknowledge the financial assistance of the South African Radio Astronomy Observatory (SARAO) towards this research (www.sarao.ac.za). LN, MH, AP, WT acknowledge support from the National Science Foundation under Grant No. 1751763. EK acknowledges support by a NASA Space Technology Research Fellowship. TCC and PB acknowledge support from the NASA Jet Propulsion Laboratory Strategic R&TD awards. Part of this work was done at Jet Propulsion Laboratory, California Institute of Technology, under a contract with the National Aeronautics and Space Administration. The research of OS is supported by the South African Research Chairs Initiative of the Department of Science and Technology and National Research Foundation. HCC acknowledges the support of the Natural Sciences and Engineering Research Council of Canada (NSERC; RGPIN-2019-04506). ADH acknowledges support from the Sutton Family Chair in Science, Christianity and Cultures and from the Faculty of Arts and Science, University of Toronto. AZ was supported by a University of Toronto Excellence Award. MGS, SP and JT acknowledge support from the South African Radio Astronomy Observatory (SARAO) and National Research Foundation (Grant No. 84156). Computations were performed

on Hippo at the University of KwaZulu-Natal, on the Baobab cluster at the University of Geneva and on the Niagara supercomputer at the SciNet HPC Consortium. SciNet is funded by: the Canada Foundation for Innovation; the Government of Ontario; Ontario Research Fund - Research Excellence; and the University of Toronto.^{67,68} This work made use of the `numpy`,⁶⁹ `scipy`,⁷⁰ `matplotlib`,⁷¹ and `astropy`^{72,73} software packages.

References

- 1 S. Alam, M. Ata, S. Bailey, *et al.*, “The clustering of galaxies in the completed SDSS-III Baryon Oscillation Spectroscopic Survey: cosmological analysis of the DR12 galaxy sample,” *MNRAS* **470**, 2617–2652 (2017).
- 2 S. Alam, M. Aubert, S. Avila, *et al.*, “Completed SDSS-IV extended Baryon Oscillation Spectroscopic Survey: Cosmological implications from two decades of spectroscopic surveys at the Apache Point Observatory,” *Phys. Rev. D* **103**, 083533 (2021).
- 3 A. Slosar, V. Iršič, D. Kirkby, *et al.*, “Measurement of baryon acoustic oscillations in the Lyman- α forest fluctuations in BOSS data release 9,” *J. Cosmology Astropart. Phys.* **2013**, 026 (2013).
- 4 DES Collaboration, T. M. C. Abbott, M. Aguena, *et al.*, “Dark Energy Survey Year 3 Results: Cosmological Constraints from Galaxy Clustering and Weak Lensing,” *arXiv e-prints*, arXiv:2105.13549 (2021).
- 5 L. Fu, M. Kilbinger, T. Erben, *et al.*, “CFHTLenS: cosmological constraints from a combination of cosmic shear two-point and three-point correlations,” *MNRAS* **441**, 2725–2743 (2014).
- 6 C. Heymans, T. Tröster, M. Asgari, *et al.*, “KiDS-1000 Cosmology: Multi-probe weak gravitational lensing and spectroscopic galaxy clustering constraints,” *A&A* **646**, A140 (2021).
- 7 C. Hikage, M. Oguri, T. Hamana, *et al.*, “Cosmology from cosmic shear power spectra with Subaru Hyper Suprime-Cam first-year data,” *PASJ* **71**, 43 (2019).
- 8 T.-C. Chang, U.-L. Pen, J. B. Peterson, *et al.*, “Baryon Acoustic Oscillation Intensity Mapping of Dark Energy,” *Phys. Rev. Lett.* **100**, 091303 (2008).
- 9 P. Bull, P. G. Ferreira, P. Patel, *et al.*, “Late-time Cosmology with 21 cm Intensity Mapping Experiments,” *The Astrophysical Journal* **803**, 21 (2015).
- 10 E. D. Kovetz, M. P. Viero, A. Lidz, *et al.*, “Line-Intensity Mapping: 2017 Status Report,” *arXiv e-prints*, arXiv:1709.09066 (2017).
- 11 K. Bandura, G. E. Addison, M. Amiri, *et al.*, “Canadian Hydrogen Intensity Mapping Experiment (CHIME) pathfinder,” in *Ground-based and Airborne Telescopes V*, L. M. Stepp, R. Gilmozzi, and H. J. Hall, Eds., *Society of Photo-Optical Instrumentation Engineers (SPIE) Conference Series* **9145**, 914522 (2014).
- 12 K. Vanderlinde, A. Liu, B. Gaensler, *et al.*, “The Canadian Hydrogen Observatory and Radio-transient Detector (CHORD),” in *Canadian Long Range Plan for Astronomy and Astrophysics White Papers*, **2020**, 28 (2019).
- 13 D. R. DeBoer, A. R. Parsons, J. E. Aguirre, *et al.*, “Hydrogen Epoch of Reionization Array (HERA),” *Publications of the Astronomical Society of the Pacific* **129**, 045001 (2017).
- 14 A. Slosar, Z. Ahmed, D. Alonso, *et al.*, “Packed Ultra-wideband Mapping Array (PUMA): A Radio Telescope for Cosmology and Transients,” in *Bulletin of the American Astronomical Society*, **51**, 53 (2019).

- 15 X. Chen, “The Tianlai Project: a 21CM Cosmology Experiment,” in *International Journal of Modern Physics Conference Series, International Journal of Modern Physics Conference Series* **12**, 256–263 (2012).
- 16 CHIME/FRB Collaboration, M. Amiri, K. Bandura, *et al.*, “Observations of fast radio bursts at frequencies down to 400 megahertz,” *Nature* **566**, 230–234 (2019).
- 17 CHIME/FRB Collaboration, M. Amiri, K. Bandura, *et al.*, “A second source of repeating fast radio bursts,” *Nature* **566**, 235–238 (2019).
- 18 CHIME/FRB Collaboration, B. C. Andersen, K. Bandura, *et al.*, “CHIME/FRB Discovery of Eight New Repeating Fast Radio Burst Sources,” *ApJ* **885**, L24 (2019).
- 19 The CHIME/FRB Collaboration, :, M. Amiri, *et al.*, “The First CHIME/FRB Fast Radio Burst Catalog,” *arXiv e-prints*, arXiv:2106.04352 (2021).
- 20 C. Ng, A. Pandhi, A. Naidu, *et al.*, “Faraday rotation measures of Northern hemisphere pulsars using CHIME/Pulsar,” *MNRAS* **496**, 2836–2848 (2020).
- 21 DESI Collaboration, A. Aghamousa, J. Aguilar, *et al.*, “The DESI Experiment Part I: Science, Targeting, and Survey Design,” *arXiv e-prints*, arXiv:1611.00036 (2016).
- 22 S. W. Henderson, R. Allison, J. Austermann, *et al.*, “Advanced ACTPol Cryogenic Detector Arrays and Readout,” *Journal of Low Temperature Physics* **184**, 772–779 (2016).
- 23 LSST Science Collaboration, P. A. Abell, J. Allison, *et al.*, “LSST Science Book, Version 2.0,” *arXiv e-prints*, arXiv:0912.0201 (2009).
- 24 R. Braun, T. Bourke, J. A. Green, *et al.*, “Advancing Astrophysics with the Square Kilometre Array,” in *Advancing Astrophysics with the Square Kilometre Array (AASKA14)*, 174 (2015).
- 25 L. B. Newburgh, K. Bandura, M. A. Bucher, *et al.*, “HIRAX: a probe of dark energy and radio transients,” in *Ground-based and Airborne Telescopes VI*, H. J. Hall, R. Gilmozzi, and H. K. Marshall, Eds., *Society of Photo-Optical Instrumentation Engineers (SPIE) Conference Series* **9906**, 99065X (2016).
- 26 M. R. Blanton, M. A. Bershad, B. Abolfathi, *et al.*, “Sloan Digital Sky Survey IV: Mapping the Milky Way, Nearby Galaxies, and the Distant Universe,” *AJ* **154**, 28 (2017).
- 27 S. Miyazaki, Y. Komiyama, H. Nakaya, *et al.*, “Hyper Suprime-Cam,” in *Ground-based and Airborne Instrumentation for Astronomy IV*, I. S. McLean, S. K. Ramsay, and H. Takami, Eds., **8446**, 327 – 335, International Society for Optics and Photonics, SPIE (2012).
- 28 L. Amendola, S. Appleby, A. Avgoustidis, *et al.*, “Cosmology and fundamental physics with the Euclid satellite,” *Living Reviews in Relativity* **21**, 2 (2018).
- 29 R. Akeson, L. Armus, E. Bachelet, *et al.*, “The Wide Field Infrared Survey Telescope: 100 Hubbles for the 2020s,” *arXiv e-prints*, arXiv:1902.05569 (2019).
- 30 B. A. Benson, P. A. R. Ade, Z. Ahmed, *et al.*, “SPT-3G: a next-generation cosmic microwave background polarization experiment on the South Pole telescope,” in *Millimeter, Submillimeter, and Far-Infrared Detectors and Instrumentation for Astronomy VII*, W. S. Holland and J. Zmuidzinas, Eds., *Society of Photo-Optical Instrumentation Engineers (SPIE) Conference Series* **9153**, 91531P (2014).
- 31 P. Ade, J. Aguirre, Z. Ahmed, *et al.*, “The Simons Observatory: science goals and forecasts,” *J. Cosmology Astropart. Phys.* **2019**, 056 (2019).
- 32 M. G. Santos, M. Cluver, M. Hilton, *et al.*, “MeerKLASS: MeerKAT Large Area Synoptic Survey,” *arXiv e-prints*, arXiv:1709.06099 (2017).

- 33 N. Gupta, R. Srianand, W. Baan, *et al.*, “The MeerKAT Absorption Line Survey (MALS),” in *MeerKAT Science: On the Pathway to the SKA*, 14 (2016).
- 34 J. S. Dillon and A. R. Parsons, “Redundant Array Configurations for 21 cm Cosmology,” *The Astrophysical Journal* **826**, 181 (2016).
- 35 K. Bandura, A. N. Bender, J. F. Cliche, *et al.*, “ICE: A Scalable, Low-Cost FPGA-Based Telescope Signal Processing and Networking System,” *Journal of Astronomical Instrumentation* **5**, 1641005 (2016).
- 36 B. R. B. Saliwanchik, A. Ewall-Wice, D. Crichton, *et al.*, “Mechanical and optical design of the HIRAX radio telescope,” in *Ground-based and Airborne Telescopes VIII, Society of Photo-Optical Instrumentation Engineers (SPIE) Conference Series* **11445**, 114455O (2021).
- 37 M. Deng and D. Campbell-Wilson, “The cloverleaf antenna: A compact wide-bandwidth dual-polarization feed for CHIME,” *arXiv e-prints*, arXiv:1708.08521 (2017).
- 38 E. R. Kuhn, B. R. B. Saliwanchik, M. Harris, *et al.*, “Design and implementation of a noise temperature measurement system for the Hydrogen Intensity and Real-time Analysis eXperiment (HIRAX),” *arXiv e-prints*, arXiv:2101.06337 (2021).
- 39 J. Mena, K. Bandura, J. F. Cliche, *et al.*, “A Radio-Frequency-over-Fiber link for large-array radio astronomy applications,” *Journal of Instrumentation* **8**, T10003 (2013).
- 40 K. Bandura, J. F. Cliche, M. A. Dobbs, *et al.*, “ICE-Based Custom Full-Mesh Network for the CHIME High Bandwidth Radio Astronomy Correlator,” *Journal of Astronomical Instrumentation* **5**, 1641004 (2016).
- 41 N. Denman, M. Amiri, K. Bandura, *et al.*, “A GPU-based Correlator X-engine Implemented on the CHIME Pathfinder,” *arXiv e-prints*, arXiv:1503.06202 (2015).
- 42 A. Recnik, K. Bandura, N. Denman, *et al.*, “An Efficient Real-time Data Pipeline for the CHIME Pathfinder Radio Telescope X-Engine,” *arXiv e-prints*, arXiv:1503.06189 (2015).
- 43 P. Klages, K. Bandura, N. Denman, *et al.*, “GPU Kernels for High-Speed 4-Bit Astrophysical Data Processing,” *arXiv e-prints*, arXiv:1503.06203 (2015).
- 44 D. Alonso, P. G. Ferreira, M. J. Jarvis, *et al.*, “Calibrating photometric redshifts with intensity mapping observations,” *Phys. Rev. D* **96**, 043515 (2017).
- 45 A. Albrecht, G. Bernstein, R. Cahn, *et al.*, “Report of the Dark Energy Task Force,” *arXiv e-prints*, astro-ph/0609591 (2006).
- 46 D. H. Weinberg, M. J. Mortonson, D. J. Eisenstein, *et al.*, “Observational probes of cosmic acceleration,” *Phys. Rep.* **530**, 87–255 (2013).
- 47 É. Aubourg, S. Bailey, J. E. Bautista, *et al.*, “Cosmological implications of baryon acoustic oscillation measurements,” *Phys. Rev. D* **92**, 123516 (2015).
- 48 A. J. Ross, L. Samushia, C. Howlett, *et al.*, “The clustering of the SDSS DR7 main Galaxy sample - I. A 4 per cent distance measure at $z = 0.15$,” *MNRAS* **449**, 835–847 (2015).
- 49 J. E. Bautista, R. Paviot, M. Vargas Magaña, *et al.*, “The completed SDSS-IV extended Baryon Oscillation Spectroscopic Survey: measurement of the BAO and growth rate of structure of the luminous red galaxy sample from the anisotropic correlation function between redshifts 0.6 and 1,” *MNRAS* **500**, 736–762 (2021).
- 50 H. Gil-Marín, J. E. Bautista, R. Paviot, *et al.*, “The Completed SDSS-IV extended Baryon Oscillation Spectroscopic Survey: measurement of the BAO and growth rate of structure of the luminous red galaxy sample from the anisotropic power spectrum between redshifts 0.6 and 1.0,” *MNRAS* **498**, 2492–2531 (2020).

- 51 A. de Mattia, V. Ruhlmann-Kleider, A. Raichoor, *et al.*, “The completed SDSS-IV extended Baryon Oscillation Spectroscopic Survey: measurement of the BAO and growth rate of structure of the emission line galaxy sample from the anisotropic power spectrum between redshift 0.6 and 1.1,” *MNRAS* **501**, 5616–5645 (2021).
- 52 A. Raichoor, A. de Mattia, A. J. Ross, *et al.*, “The completed SDSS-IV extended Baryon Oscillation Spectroscopic Survey: large-scale structure catalogues and measurement of the isotropic BAO between redshift 0.6 and 1.1 for the Emission Line Galaxy Sample,” *MNRAS* **500**, 3254–3274 (2021).
- 53 J. Hou, A. G. Sánchez, A. J. Ross, *et al.*, “The completed SDSS-IV extended Baryon Oscillation Spectroscopic Survey: BAO and RSD measurements from anisotropic clustering analysis of the quasar sample in configuration space between redshift 0.8 and 2.2,” *MNRAS* **500**, 1201–1221 (2021).
- 54 R. Neveux, E. Burtin, A. de Mattia, *et al.*, “The completed SDSS-IV extended Baryon Oscillation Spectroscopic Survey: BAO and RSD measurements from the anisotropic power spectrum of the quasar sample between redshift 0.8 and 2.2,” *MNRAS* **499**, 210–229 (2020).
- 55 H. du Mas des Bourboux, J. Rich, A. Font-Ribera, *et al.*, “The Completed SDSS-IV Extended Baryon Oscillation Spectroscopic Survey: Baryon Acoustic Oscillations with Ly α Forests,” *The Astrophysical Journal* **901**, 153 (2020).
- 56 Planck Collaboration, N. Aghanim, Y. Akrami, *et al.*, “Planck 2018 results. VI. Cosmological parameters,” *A&A* **641**, A6 (2020).
- 57 D. M. Scolnic, D. O. Jones, A. Rest, *et al.*, “The Complete Light-curve Sample of Spectroscopically Confirmed SNe Ia from Pan-STARRS1 and Cosmological Constraints from the Combined Pantheon Sample,” *The Astrophysical Journal* **859**, 101 (2018).
- 58 T. M. C. Abbott, F. B. Abdalla, A. Alarcon, *et al.*, “Dark Energy Survey year 1 results: Cosmological constraints from galaxy clustering and weak lensing,” *Phys. Rev. D* **98**, 043526 (2018).
- 59 J. R. Shaw, K. Sigurdson, U.-L. Pen, *et al.*, “All-sky Interferometry with Spherical Harmonic Transit Telescopes,” *The Astrophysical Journal* **781**, 57 (2014).
- 60 J. R. Shaw, K. Sigurdson, M. Sitwell, *et al.*, “Coaxing cosmic 21 cm fluctuations from the polarized sky using m-mode analysis,” *Phys. Rev. D* **91**(8), 083514 (2015).
- 61 A. Liu and J. R. Shaw, “Data Analysis for Precision 21 cm Cosmology,” *Publications of the Astronomical Society of the Pacific* **132**, 062001 (2020).
- 62 M. G. Santos, A. Cooray, and L. Knox, “Multifrequency Analysis of 21 Centimeter Fluctuations from the Era of Reionization,” *The Astrophysical Journal* **625**, 575–587 (2005).
- 63 C. G. T. Haslam, C. J. Salter, H. Stoffel, *et al.*, “A 408 MHz all-sky continuum survey. II. The atlas of contour maps,” *A&AS* **47**, 1–143 (1982).
- 64 CHIME/FRB Collaboration, M. Amiri, K. Bandura, *et al.*, “The CHIME Fast Radio Burst Project: System Overview,” *The Astrophysical Journal* **863**, 48 (2018).
- 65 M. Amiri, K. M. Bandura, P. J. Boyle, *et al.*, “The CHIME Pulsar Project: System Overview,” *ApJS* **255**, 5 (2021).
- 66 J. Mena Parra *et al.*, “A clock stabilization system for CHIME/FRB Outriggers,” (in preparation).

- 67 C. Loken, D. Gruner, L. Groer, *et al.*, “SciNet: Lessons learned from building a power-efficient top-20 system and data centre,” *Journal of Physics: Conference Series* **256**, 012026 (2010).
- 68 M. Ponce, R. van Zon, S. Northrup, *et al.*, “Deploying a top-100 supercomputer for large parallel workloads: The niagara supercomputer,” in *Proceedings of the Practice and Experience in Advanced Research Computing on Rise of the Machines (Learning)*, PEARC ’19, Association for Computing Machinery, (New York, NY, USA) (2019).
- 69 C. R. Harris, K. J. Millman, S. J. van der Walt, *et al.*, “Array programming with NumPy,” *Nature* **585**, 357–362 (2020).
- 70 P. Virtanen, R. Gommers, T. E. Oliphant, *et al.*, “SciPy 1.0: Fundamental Algorithms for Scientific Computing in Python,” *Nature Methods* **17**, 261–272 (2020).
- 71 J. D. Hunter, “Matplotlib: A 2d graphics environment,” *Computing in Science Engineering* **9**(3), 90–95 (2007).
- 72 Astropy Collaboration, T. P. Robitaille, E. J. Tollerud, *et al.*, “Astropy: A community Python package for astronomy,” *A&A* **558**, A33 (2013).
- 73 Astropy Collaboration, A. M. Price-Whelan, B. M. Sipőcz, *et al.*, “The Astropy Project: Building an Open-science Project and Status of the v2.0 Core Package,” *AJ* **156**, 123 (2018).

List of Figures

- 1 HIRAX will observe $\sim 15,000 \text{ deg}^2$ of the southern sky, shown by the region enclosed by the white dashed lines. The survey footprint overlaps many existing and forthcoming surveys such as those of CHIME,¹¹ DES,⁴ KiDS,⁶ DESI²¹ and Advanced ACTPol.²² The entirety of the sky area shown is contained within the Rubin/LSST²³ survey footprint and is accessible to the SKA²⁴ and its precursors. The background colorscale shows Galactic emission from the *Planck* 353 GHz map.
- 2 Artist’s impression of the HIRAX array in the Karoo desert.
- 3 HIRAX signal chain schematic. In each dish, an active dual-polarization feed receives and amplifies incoming radio signals. The signals are filtered, further amplified, and converted to optical light with an RFoF transmitter at the dish focus. Optical fibre transports the signals to an RFoF receiver, which converts the signals back into RF and applies additional amplification and filtering before digitization. An ICE-based system performs the digitization, channelizing, and corner turn. The data are then passed to the GPU X-engine for correlation.

- 4 (a) Angular scales accessible to HIRAX baselines as a function of frequency. The background colour scale represents the BAO feature in the 21 cm power spectrum assuming line-of-sight modes, k_{\parallel} , corresponding to correlations over 15 MHz in frequency. The blue curve shows approximately where non-linear effects become significant. This demonstrates the importance of HIRAX's short baselines, and hence compact layout, for measuring the BAO feature. (b) Comparison of HIRAX's power spectrum sensitivity as a function of k_{\perp} with that of SKA-MID surveys, in single dish (SD) and interferometer (IF) mode, shown alongside shot noise estimates from upcoming spectroscopic galaxy surveys from DESI, Euclid and Roman. The upper panel shows the BAO feature in the power spectrum as a function of k_{\perp} at $z = 1.2$. Differences in sensitivity due to different survey areas, and hence cosmic variance contributions, are not accounted for here.
- 5 Forecast constraints on (a) the BAO feature of the matter power spectrum, (b) distance scale, D_V evolution, (c) dark energy equation of state parameters w_0 and w_a , (d) large-scale structure parameters σ_8 and Ω_M , for HIRAX-256 and HIRAX-1024. Parameter contours shown represent 68% confidence intervals and, for the parameter constraints, a prior based on *Planck*⁵⁶ results has been added. We note that the change in degeneracy direction for the Ω_M and σ_8 contours between HIRAX-256 and HIRAX-1024 is due to the different relative contributions of the *Planck* prior to the combined constraints.
- 6 Estimated relative errors in recovered $P(k_{\parallel}, k_{\perp})$ band-powers (from diagonal elements of the derived covariance matrices) over 100 MHz sub-bands spanning the HIRAX bandwidth using the *m*-mode pipeline. A foreground filter has been applied here assuming ideal knowledge of the instrument.

List of Tables

- 1 HIRAX instrument parameters for the initial 256-element array.
- 2 HIRAX-256 correlator node specifications. The HIRAX-256 X-engine is comprised of eight these nodes.
- 3 Marginalized 68% cosmological parameter forecast constraints for the HIRAX experiment compared to current eBOSS² results for Λ CDM, w CDM and w_0w_a CDM cosmologies.
- 4 Target precision values for HIRAX telescope mechanical structure